Gas-driven fracturing of saturated granular media

James M. Campbell, Deren Ozturk, Bjørnar Sandnes*
College of Engineering, Swansea University, Bay Campus, Fabian Way, Swansea SA1 8EN, UK.

Multiphase flows in deformable porous materials are important in numerous geological and geotechnical applications, however the complex flow behaviour make subsurface transport processes difficult to control or even characterise. Here we study gas-driven (pneumatic) fracturing of a wet unconsolidated granular packing confined in a Hele-Shaw cell, and present an in-depth analysis of both pore-scale phenomena and large-scale pattern formation. The process is governed by a complex interplay between pressure, capillary, frictional and viscous forces. At low gas injection rate, fractures grow in a stick-slip fashion and branch out to form a simply connected network. We observe the emergence of a characteristic length-scale – the separation distance between fracture branches – creating an apparent uniform spatial fracture density. We conclude that the well defined separation distance is the result of local compaction fronts surrounding fractures, keeping them apart. A scaling argument is presented that predicts fracture density as a function of granular friction, grain size, and capillary interactions. We study the influence of gas injection rate, and find that the system undergoes a fluidisation transition above a critical injection rate, resulting in directional growth of fractures, and a fracture density that increases with increasing rate. A dimensionless Fluidisation number F is defined as the ratio of viscous to frictional forces, and our experiments reveal a frictional regime for $F < 1$ characterized by stick-slip, rate independent growth, with a transition to a viscous regime ($F > 1$) characterized by continuous growth in several fracture branches simultaneously.

INTRODUCTION

Multiphase fracturing whereby a gas penetrates a liquid-saturated granular or colloidal material occurs in a wide range of natural and engineered processes. Polygonal mudcracks in soils and crack patterns in paint are familiar examples of emergent pattern formation where fractures are forced open by capillary interactions as the material shrinks when it dries [1–3]. Methane venting through sediments represents a significant source of greenhouse gas emission to the atmosphere [4]. Methane flux rates are intimately linked with complex gas migration in the form of rising bubbles or fractures, deforming the sediment and causing intermittent venting from localized conduits and pockmarks on the ocean floor [5–11]. Other examples from nature include volcanoes and magmatic systems, where migration of gas (volatiles) through a mush of crystals and melt influence eruption behaviour and the escape of large amounts of gases to the atmosphere [12, 13]. Gas-driven fracturing and deformation of the crystal matrix creates conductive pathways for migration of volatiles through the mush, which can explain the episodic eruptive bursts characteristic for some volcanic systems (e.g. Stromboli), and why crystal rich magmas often are found to have depleted volatile fractions [13–15].

In industry, gas-driven fracturing of soil and porous media is a key process in stimulation of sensitive hydrocarbon reservoirs [16, 17], pneumatic fracturing for enhanced remediation of contaminated soil [18, 19], and carbon dioxide injection and storage in subsurface reservoirs [20, 21]. Gas-driven (pneumatic) fracturing differs from the well-known process of hydraulic fracturing—or "fracking"—used to extract shale gas and oil. Gas-driven fracturing is a complex process that involves multiphase flow of gas/liquid/grains whereas hydraulic fracturing typically features a single-phase flow of a water-based fracturing fluid. The presence of a gas-liquid interface at the fracture boundary means that capillary forces play an important role in shaping the fracture growth dynamics [6, 22–26].

Multiphase fluid flow and fracturing processes are poorly understood on a fundamental level. Fluid instabilities involving viscous, capillary and frictional forces, together with pore-scale disorder and evolving matrix geometries, result in a wide range of flow patterns and possible fracturing outcomes. From an applied point of view, the inherent complexity, and the current lack of fundamental scientific insight, makes fluid-driven fracturing processes difficult to control, with often unpredictable results in terms of permeability generation.

Here we study a simple model system: the fracturing of a water-saturated, non-cohesive granular medium by the forced injection of pressurized air. In order to observe the fracturing dynamics, we study a thin layer of material confined between two parallel glass plates: a Hele-Shaw cell. Amongst the first uses of the Hele-Shaw cell was to demonstrate viscous fingering, a branching instability apparent when injecting a low viscosity fluid into one of higher viscosity [27–32]. There have been many different approaches to incorporating granular material into such a system, and all produce distinct and often visually striking flow patterns [22, 33–38]. In each case the driving force behind pattern formation is the complex interplay and competition between fluid flow, bead-bead friction and capillary forces.

The invasion of air into a liquid which is only partially filled with granular material results in a particularly rich set of patterns: from viscous fingers to bubbles

to labyrinthine structures [39–42]. Results are dominated by fronts of dense granular material which accumulate ahead of interfaces, retarding advancement by means of friction. In contrast, if the cell contains a granular material which is held rigidly in place then capillary invasion is observed between the grains, or viscous fingering at very high injection rates [26, 43–45]. Fracturing occurs between these two extremes: when the cell is fully packed with granular material but not so tightly packed that the grains are immobile.

Multiphase fracturing in granular media has been observed before [21, 22, 25, 26, 41, 46–48]. Chevalier *et al.* observed a transition from viscous fingering to a fracture-like invasion pattern in very dense granular suspensions [22]. Holtzman *et al.* mapped a transition between viscous/capillary fingering and "capillary fracturing", and showed that the transition depended on the competition between a local fracturing pressure and the frictional resistance which in turn depended on the confining pressure [26]. Sandnes *et al.* proposed a phase diagram of displacement morphologies for gas intrusion in materials ranging from consolidated porous media to loose granular mixtures, with fracturing as the dominant morphology for systems with intermediate filling fraction [41].

It must be noted that the process referred to as "fracturing" throughout this and other works (the invasion of a gas into a saturated granular material in the form of narrow channels) is fundamentally different to more conventional fracturing of elastic and cohesive materials such as metals and rocks (separation of a previously continuous solid phase due to tensile stress). In the capillary fracturing process described here, there are no cohesive bonds between the grains, and the fracture-like shape of the invasion front is a result of pressure and capillary forces acting at the fracture interface, and frictional forces acting between grains, and between grains and the confining boundary.

Here we present several new insights into how gas-driven, capillary fractures nucleate and grow, and the effect of granular material properties and injection rate on the morphology of the fracture patterns. First we demonstrate that the fractures nucleate by pore invasion, and that the growth of a fracture branch is associated with a compaction of the granular packing surrounding the branch. We show that the thickness of this compaction front can be predicted from the characteristics of the granular material (size and shape), and that the compaction fronts in turn determine the spatial density of the final fracture pattern. Subsequently we find that the patterns are rate-independent below a fluidisation threshold, above which we demonstrate a transition to a viscous regime where the fractures align with the fluid flow streamlines, and the fracture density increases with increasing injection rate.

MATERIALS AND METHODS

Experimental setup

Experiments were performed in a Hele-Shaw cell, as shown in Figure 1 (a). Two 350×350×18 mm glass plates were held together by 0.5 mm adhesive plastic spacers; these sealed three sides of the cell, leaving a 200 mm-wide channel which was open at one end. A hole was drilled through one of the plates providing an inlet at the closed end of this channel, 300 mm from the open end.

A bed of loosely packed glass grains was formed within the cell by turning it vertically, filling it with deionised water and pouring the grains into the top of the channel to sediment downwards. A head of water of about 1 cm was left between the top of the granular bed and the end of the cell to prevent evaporation from influencing results.

After the bed had fully settled, the cell was turned horizontal. Air was injected into the inlet at various rates using a syringe pump (Harvard Scientific, PHD Ultra), while a pressure sensor (Sensortechnics) logged the relative air pressure at 5 Hz. No pressure log was taken at rates above 10 mL·min^{-1} as the pressure rose above the range of our instrument. Injection was initially done at a slow rate (0.03 mL·min^{-1}) to push through excess water in the inlet without disturbing the grain packing; afterwards (but before the appearance of the first fracture) the rate was raised or lowered to the rate of interest and held there for the duration of the experiment. Photographs were taken at regular intervals to record the results. A gas injection volume of 8 mL was used for all experiments presented here. The edge of the channel was kept unobstructed (open boundary conditions) in all experiments.

Both spherical beads and rough, irregular grains of soda-lime glass were used as shown in Figure 1 (b) and (c), sieved to various size ranges between 53 and 250 μm. The bead beds had measured initial porosities η_0 between 0.415 and 0.465 (increasing with increasing bead size due to edge effects), consistent with values expected for a random loose packing of spheres [49]. Irregular grains, which were sieved to 75–100 μm, packed with a significantly higher porosity of $\eta_0 = 0.63$. Both beads and irregular grains were washed in a 3:1 mixture of sulphuric acid and hydrogen peroxide (piranha solution), and rinsed thoroughly in deionised water prior to use. The piranha solution treatment ensures removal of contamination and a highly wetting, hydrophilic surface. Piranha treated soda-lime glass is estimated to have an air-water-glass contact angle of $\theta = 12 \pm 5^\circ$ [50]. Bed porosity was determined by finding the mass of granular material needed to fill a known volume of the cell. Permeability was found by measuring the pressure difference needed to push water through the bed at 0.03 mL·min^{-1}, which relates to

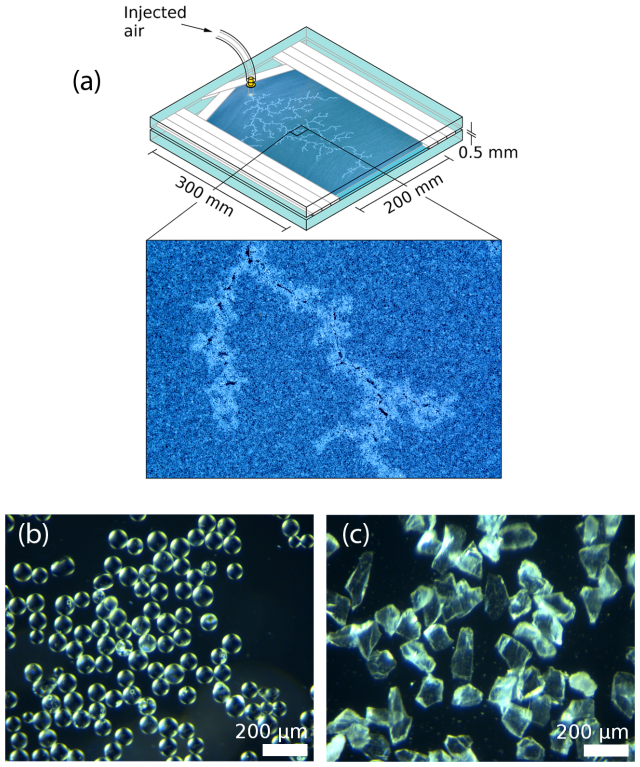

FIG. 1. Experimental setup. (a) Through an inlet, air invades the water-saturated granular packing in a branching fracture pattern. (b) Spherical beads and (c) irregular grains used in the study, both sieved between 75 and 100 μm.

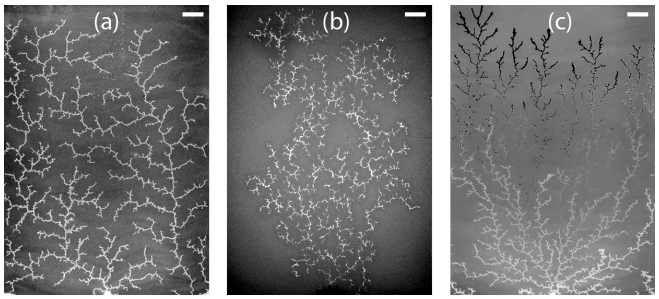

FIG. 2. Growth of gas fractures in saturated granular media. (a) Video 1: 53-100 μ m spherical beads, injection rate 0.03 ml/min. The actively growing fracture tips are highlighted in black. (b) Video 2: 75-100 μ m irregular grains, injection rate 0.03 ml/min (c) Video 3: Fracture growth at high injection rate. 53-100 μ m spherical beads, injection rate 10.0 ml/min. Scale bar is 2 cm in all panels.

the permeability by Darcy's law [51].

Figure 2 shows illustrative examples of the fracturing dynamics at low injection rate for spherical beads (a) and irregular grains (b), as well as fracturing at high rate (c).

Data and image analysis

Fracture patterns were analysed at the moment they first reached 20 cm from the inlet to avoid edge effects. For comparisons between rates, 15 cm was instead used for the cut-off due to fluidization of the granular packing close to the edge of the cell at high rates. Image subtraction, thresholding and despeckling were applied in sequence to produce the binary images presented here. A binary closing operation was then used to remove small holes, after which the total length of the fractures was found as half the perimeter of the pattern. To find the branching properties, the pattern was skeletonised after manually correcting any remaining gaps in the image. A custom algorithm then translated the skeletonised image into a logical branching structure, removing any detail on scales below 1 mm.

Fracture density was measured as the fracture pattern length divided by the area of the convex hull of the pattern. Mean cross-sectional area of the fractures was found by using the pressure log and known injection rate to infer the total volume of invaded gas, and dividing this by the total fracture length. The peak pressure is simply the highest gas pressure achieved during the course of the experiment. We define tortuosity as the ratio between the direct Cartesian distance to the inlet and the distance following the path of the fractures; the mean tortuosity is merely this averaged over the whole pattern.

To study the system dynamics in more detail, a smaller region was observed in the centre of the cell at higher magnification and at 60 frames per second. Particle Image Velocimetry (PIV) was performed on the images using the OpenPIV software package.

RESULTS AND DISCUSSION

Fracture growth in the frictional regime at low injection rate

This section describes the dynamics of fracture growth at injection rates of 0.1 mL/min and below. A later section discusses the rate dependence of the process.

Figure 3 (a) shows a time series of typical fracture growth for 53–100 μm spherical beads. The injected air invades the granular bed by opening a branching pattern of narrow fractures, typically never more than three bead diameters wide. The pattern has an apparently random bifurcating structure with branches opening by a process of tip-splitting. The fractures never intersect each other. Figure 3 (b) shows the growth dynamics for a full fracture pattern coloured according to formation time. Fractures are sometimes seen to grow preferentially along the edge of the packing. This is likely an effect of locally inefficient packing close to the walls.

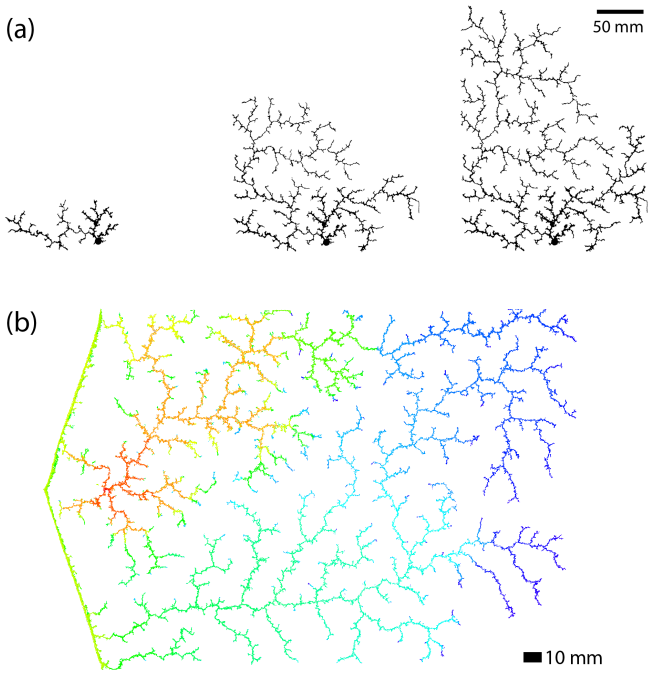

FIG. 3. Fracture growth. (a) Thresholded images of fracture pattern at $\Delta t = 350$ s time intervals. (b) Fracture pattern coloured by formation time. (c) Gas pressure (black line) alongside fracture growth rate derived from image sequence (coloured bars), showing stick-slip behaviour characterised by short bursts of rapid growth. Colour scales in (b) and (c) are identical. (Injection rate $q = 0.03$ mL/min, 53–100 μm beads.)

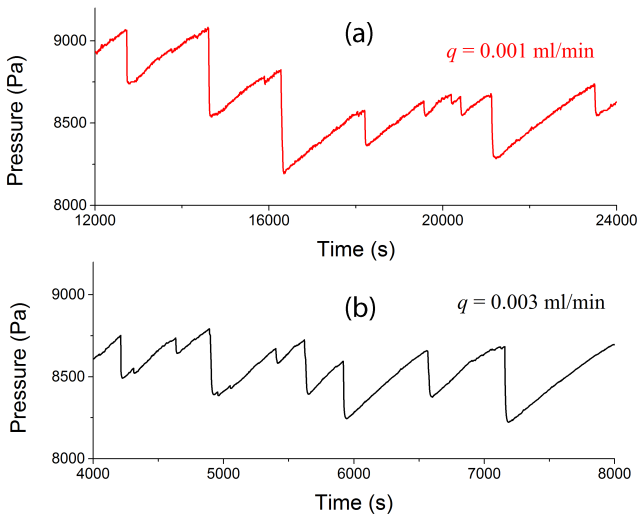

FIG. 4. Gas pressure during stick slip fracturing for (a) 0.001 mL/min, and (b) 0.003 mL/min. The time axis shows a three times longer duration for (a) compared to (b).

Figure 3 (c) shows the variation in gas pressure alongside the fracture growth rate over the course of a typical experiment. Although the gas is injected at a constant rate, the fracturing is intermittent, with periods of inactivity during which the pressure builds, and short bursts of rapid growth. Such behaviour is common in friction-dominated systems such as stick-slip sliding [52], earthquakes [53] and granular avalanches [54]. It is to be supposed that grain-grain and grain-cell friction hold back fracture expansion until a threshold pressure is achieved, at which point there is rapid growth curtailed by a consequent pressure drop. Up to 0.1 mL/min, the gas injection rate has little or no impact on the magnitude of these slip events but rather determines the length of the stick periods between slips, as demonstrated in Figure 4.

Figures 5 (a)–(c) look in more detail at the dynamics of a single slip event. One sudden drop in pressure is often seen to be the result of the almost simultaneous growth of several lengths of fracture, usually local but disconnected from one another. We conclude that a single slip event causes a chain reaction in neighbouring regions that are close to their threshold pressure, caused by fluid flow induced disturbance of the packing in the vicinity of a growing fracture. Figure 5 (c) shows that the seven active branches nucleated in sequence within a 0.5 s time window during this particular slip event. Fracture growth comes to a halt after 1–2 s.

Granular compaction fronts

Particle Image Velocimetry (PIV) analysis was performed on growing fractures and an illustrative result is presented in Figure 6. The fracture pushes grains ahead of it and to either side, creating a compacted front beyond which the packing is unperturbed. An applied force to a thick compacted front will be propagated to the out-of-plane confining walls via force chains within the material [55, 56], causing it to jam [57–59] and stop the fracture from expanding. Such compaction fronts have been observed before in frictional fingering experiments where the Hele-Shaw cell is only partially filled with granular material [39, 41]. Chevalier *et al.* studied fracturing of density matched granular suspensions, and found that the mobilization of grains occurred in the local vicinity of the advancing fracture tip for suspensions with high granular volume fraction [22].

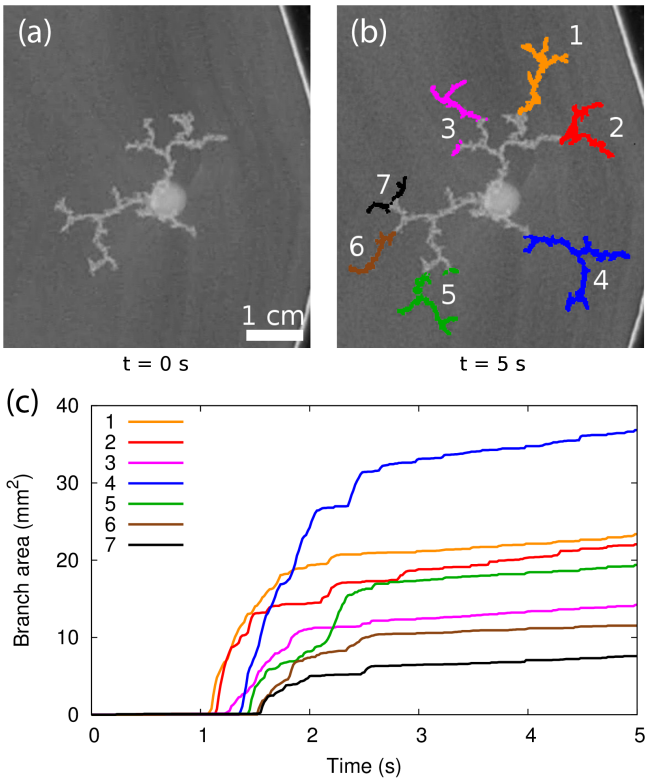

FIG. 5. (a) and (b) show images of a fracture pattern five seconds apart during 0.01 mL/min injection. The growth area is divided into seven disconnected regions and labelled. (c) Variation of area of each region with time between above images, from analysis of video footage, showing synchronized growth after a prolonged stationary period.

Figures 7 (a)–(c) show an individual fracture with associated grain displacement field and granular bed density relative to the initial packing density. The analysis reveals the local compaction zone (red halo) surrounding the fracture. The resolution of the PIV data is insufficient to resolve the narrow width of the gas filled fracture, producing an exaggerated decompaction zone (blue colour). Figure 7 (d) shows the percentage compactivity measured as a function of distance to the nearest fracture branch, averaged over three separate fracture events. The local compaction of the granular material absorbs the deformation caused by the growing fracture. Thus, a key requirement for fracturing of a deformable porous medium is compactibility. We define compaction Ξ as

$$\Xi = \frac{n_0 - n_c}{1 - n_0}, \tag{1}$$

where n_c and n_0 are the compacted and uncompacted granular bed porosities respectively. From Figure 7 (d) we can make a rough estimate of $\Xi \approx 0.7\%$ as the peak value of the median compaction for 53–100 μm beads.

The existence of these compaction fronts explains the self-avoiding nature of the fracture patterns: fractures

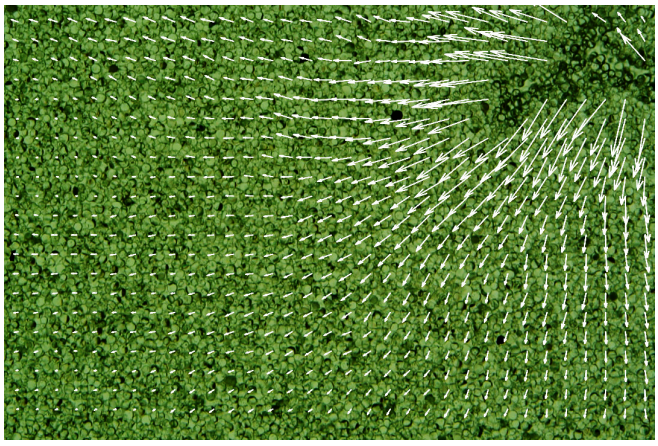

FIG. 6. Close-up during growth of a fracture from the top right corner. Granular displacement vectors from PIV analysis show large deformation close to the growing fracture. Bead diameter: 150 - 200 μm.

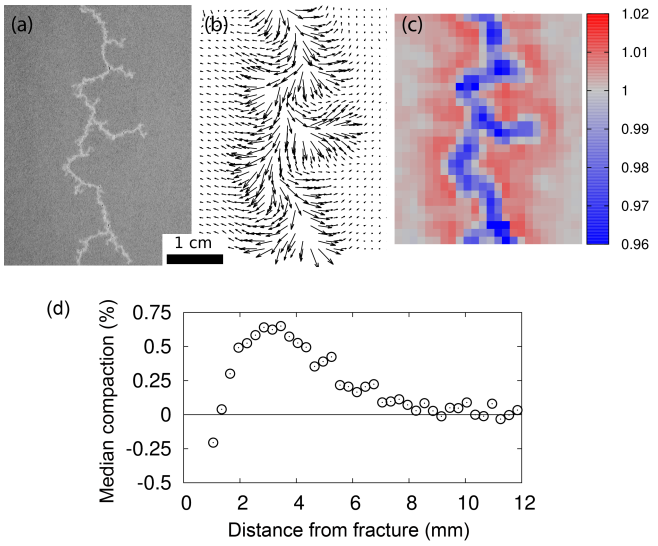

FIG. 7. Compaction fronts. (a) Photograph of a fracture in 53–100 μm beads which propagated from top to bottom of the image, 0.1 mL/min. (b) Grain displacement field, exaggerated 50×. (c) Granular bed density relative to that at start of experiment, found from the divergence of the displacement field. Red areas show compaction, blue areas expansion. (d) Compaction data from three images such as (c) was binned by distance to the nearest fracture; this graph presents the median compaction as function of distance from fracture.

cannot grow into the already compacted regions around existing fractures. The total cross-sectional width occupied by a fracture comprises the width W of the (gas-filled) fracture itself and the compaction fronts either side, each of a thickness L. The length $W + 2L$ thus sets a lower limit for the spacing between separate, parallel fracture branches. Fractures may not necessarily approach one another as close as this, but they may approach no closer.

Observing the fully developed fracture patterns displayed in Figure 3, the patterns appear to fill the available space surprisingly efficiently for a random branching structure. The patterns appear fractal on small scale, but on the scale of the cell, a characteristic separation length between the fracture branches can be discerned. The pattern is more "space filling" than "fractal", and there is in Figure 3 never more than about a centimetre separating the bulk of the porous medium from the nearest fracture branch.

The emergence of a characteristic length implies that the system displays a well-defined spatial fracture density D. We define D as the length of fracture per unit area of invaded porous media, and hypothesize that D emerges as a consequence of the separation of fractures due to their compaction fronts. To explore this concept further, we introduce a minimalist model for fracture density, where D represents the inverse of the minimum separation distance due to the space occupied by fractures and their compaction fronts:

$$D = \frac{1}{W + 2L}. \tag{2}$$

Conceptually, D is equivalent to the spatial frequency of straight, parallel fractures separated by two compaction fronts, i.e. maximally efficient invasion of the granular bed. If the compaction (Eq. 1) of the porous material is known, then the fracture width may be expressed as $W = 2\Xi L$, such that $D = [2(1 + \Xi)L]^{-1}$.

This minimalist model will in a later section be developed to provide a prediction of fracture density from basic material properties, but for now consider Figure 7 (d) which gives a rough estimate of the distance at which compaction drops below 50% of its maximum value as 5.5 mm for 53–100 μm beads. This implies a minimum separation distance of $W + 2L = 11$ mm, i.e. a fracture density of $D \approx 0.9$ cm^{-1}, which is in good agreement with measured values of ~ 1 cm^{-1}. (Experimental measurements of D will be presented in more detail in a later section).

It can be imagined that in a confined, closed system fractures will eventually grow into unprocessed regions until all the available space is either occupied by fractures, their corresponding fracture fronts, or spaces too small to hold a fracture and its fronts. As such, closed systems would be expected to display fully fractured beds with well-defined fracture densities.

However, the setup we have used has an open boundary so the reason why the fracture network grows to fill space, rather than produce the fractal structures typically seen in e.g. viscous/capillary fingering in porous media, is not immediately obvious. It is possible that the partial confinement (channel geometry) may enhance the space-filling tendency compared to previous studies of fracturing from a central inlet where the fractures can spread out laterally in all directions [14, 26, 60]. Also, buoyancy effects in vertical cells [9, 21, 23] and viscous effects at higher injection rate [22] may significantly affect the pattern formation.

The dynamics of fracturing could itself promote a space-filling pattern. Consider Figure 5, where disturbance from fracture growth in one branch is seen to trigger the nucleation of additional fractures nearby. It seems likely that this cooperative action has the effect of creating a "process zone" of multiple fracturing events in the locality of the initial fracture nucleation. Thus the active growth region becomes fully invaded by the concurrently growing fractures, producing a pattern that is space-filling on a local scale. Fractal growth may still exist, but at a larger scale than that observed in these experiments.

Note that the patterns showed considerable variability, with patches incompletely filled by fractures (see 8 and Figure 12). The space-filling nature of the pattern is however evident in the fractured regions of the cell.

Effect of grain size

Figure 8 (a) shows fracture patterns for different size ranges of spherical beads. Although there is variability in the overall shape of the patterns, the fracture density in the fractured zones appears relatively insensitive to the grain size. The open circles in Figure 8 (b) depict the measured fracture density, and reveals an overall trend of a slightly increasing D as a function of grain size. The exception is the lowest grain size (53–75 μm) where the experiment suffered from an artefact whereby the air invaded the space between the top glass plate and the granular bed, especially around the inlet. This effect is noticeable as dark patches in the lower part of the experiment shown in Figure 8 (a) (left).

While the pattern morphology appears relatively insensitive to grain size, this is not the case for the gas pressure at the point of fracturing which is observed to decrease with increasing grain size (Figure 8 (b) red diamonds). The red line is a fit to the Laplace pressure equation for the pressure difference δP across a spherical interface [51]:

$$\delta P = a\frac{4\gamma \cos\theta}{d} \tag{3}$$

where γ is the surface tension of water (0.072 N/m), d is the diameter of the beads, and θ is the contact angle, for which we used a value of 12° [50]. a is the free variable in the fit and is found to be 2.14 for the peak pressures as shown, with a lower value of approximately 2.0 for the average pressures at the onset of fracturing. Physically, this means that the measured fracturing pressure is equivalent to that needed to invade a hydrophilic cylindrical pore of diameter roughly half that of the beads.

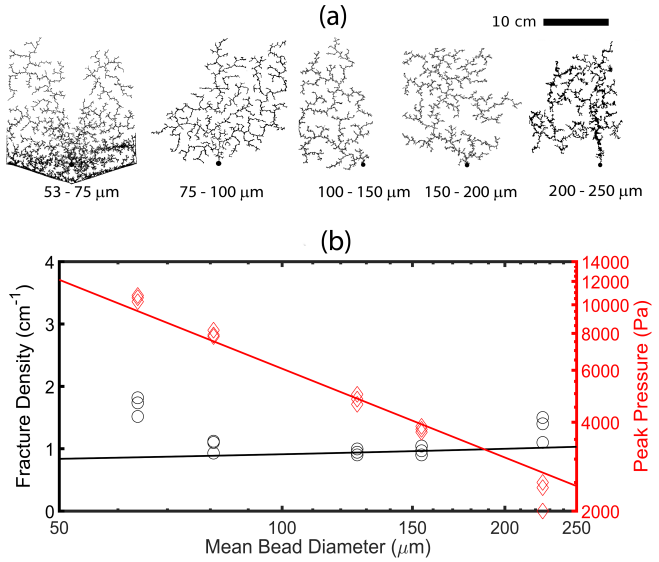

FIG. 8. Effect of bead size. (a) Fracture patterns, and (b) fracture density (black circles) and peak pressure (red diamonds) as a function of measured mean bead diameter. Each symbol represents a single experiment. The black line shows the density predictions of Equation 7. The red line shows a fit of the peak pressure to a d^{-1} dependency.

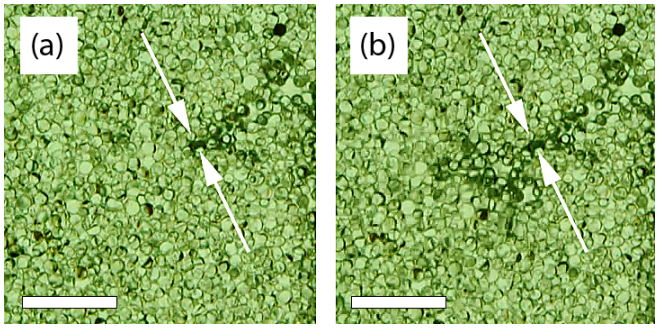

FIG. 9. Onset of fracture growth. (a) and (b) show images taken at a 0.08 s time interval, with a new fracture starting to grow towards the lower left hand corner. Arrows point to stationary beads as the fracture nucleates by capillary invasion of the compacted front. Bead diameter: 150 - 200 μm. Scale bar: 1 mm

Once a compaction front is established, it cannot simply be pushed out of the way by a higher pressure: this merely causes it to compact the grains behind it, thickening the front, as observed in simulation [61]; rather a fracture must somehow breach through the front. The pressure triggering the onset of fracturing corresponds to an interface curvature roughly 2.0 times that of the grains. For comparison, one study of pore throats in a random close packing of equal spheres (we assume that in the compaction front the grains are close packed) found the ratio between the maximum interface curvature and the sphere curvature to begin at 1.8 for the very widest pores in the system [62]. By this measure our fracturing pressure is close to the pressure at which we would expect capillary invasion into the largest available pores. Capillary invasion between the grains in the static compaction front is thus the trigger for the nucleation of a new fracture. The fluid flow from the capillary invasion is sufficient to briefly mobilise the packing, leading to a self-reinforcing process of invasion causing flow leading to bead mobilisation that triggers rapid invasion of air in the form of fractures. Figure 9 shows the point of nucleation of a new fracture branch. The beads in the initial compaction front remain largely undisturbed as the gas penetrates the front by pore invasion. As the invading gas emerges on the other side of the compaction front, the packing is mobilized, and the fracture expands by pushing grains ahead and to the sides.

The concept of capillary fracturing described above follows that of previous work by other authors [6, 24, 26], but for a subtle difference: The emergence of the compaction front requires the pressure to exceed the capillary pore entry pressure of the close-packed material in the front. It is not enough for the capillary forces to exceed the deformation- or frictional resistance of the undisturbed medium. Instead there is a feedback effect where the thickness of the compaction front grows to balance the gas pressure, forcing the pressure to increase to the point of capillary invasion (without necessarily disturbing the grain configuration). Fracturing as observed in the experiments presented here is thus a two stage process: initial capillary invasion followed by deformation and fracturing, where the required pressure is always set by the pore entry pressure of the close-packed material of the compaction front, regardless of the frictional properties of the medium.

Effect of granular friction (grain shape)

The effect of grain shape was studied by comparing spherical beads with irregular, rough grains (as seen in Figure 1), both sieved to a narrower distribution of 75–100 μm. The same PIV analysis as performed for Figure 7 was used to reveal the differences in the compaction fronts between the two grain shapes, as shown in Figure 10.

It can be seen in Figure 10 (a) that the peak compaction value for the irregular grains is much higher than that for the spherical beads, 1.3% and 0.4% respectively. This higher compaction is explained by the packing of irregular grains having a greater porosity than the packing of spherical beads (0.63 compared to 0.43), and with more degrees of freedom, there is a greater potential for reconfiguration and compaction. The measured permeability of the irregular grains (295×10^{-9} cm^2) was also larger than for the same sized 75–100 μm beads (72×10^{-9} cm^2), suggesting the irregular grains do have large pore spaces on average for their size.

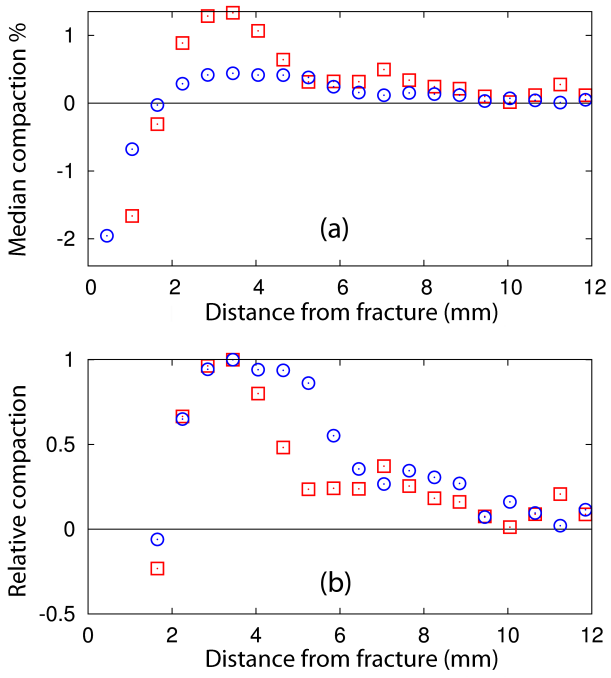

FIG. 10. (a) Median compaction at each distance for 75–100 μm spherical beads (blue circles) and irregular grains (red squares). (b) The same data normalised relative to the maximum compaction for each grain type, showing the varying widths of the compaction fronts.

Figure 10 (b) shows that the compaction front is narrower for the irregular grains: ≈4.5 mm compared to ≈6 mm for spherical beads. This is because the irregular grains will have a higher effective friction against the cell walls than the smooth beads, meaning a narrower front is needed to hold back the same pressure. As an indirect measure of frictional properties, the angle of repose α for dry irregular grains was measured to be 45°, compared to 32° for spherical beads.

As a consequence of having narrower compaction fronts, it should be expected that fractures in irregular grains will be able to approach closer to each other than those in spherical beads, increasing the fracture density D in the system. This result is observed in the fracture patterns shown in Figure 11, where the irregular grains in (b) are seen to form a denser pattern than the spherical beads in (a). Measurements of fracture density (fracture length divided by convex hull) on three replicate experiments on each grain type (Figure 11 (e)) show that irregular grains indeed display a higher average fracture density of 1.4 cm^{-1} compared to 1.0 cm^{-1} for the spherical beads.

The measured gas pressure at the onset of fracturing (red triangles in Figure 11 (e)) is considerably lower for the irregular grains (3500 kPa compared to 8500 kPa for spherical beads). This observation supports the explanation presented in the previous section that the fracturing

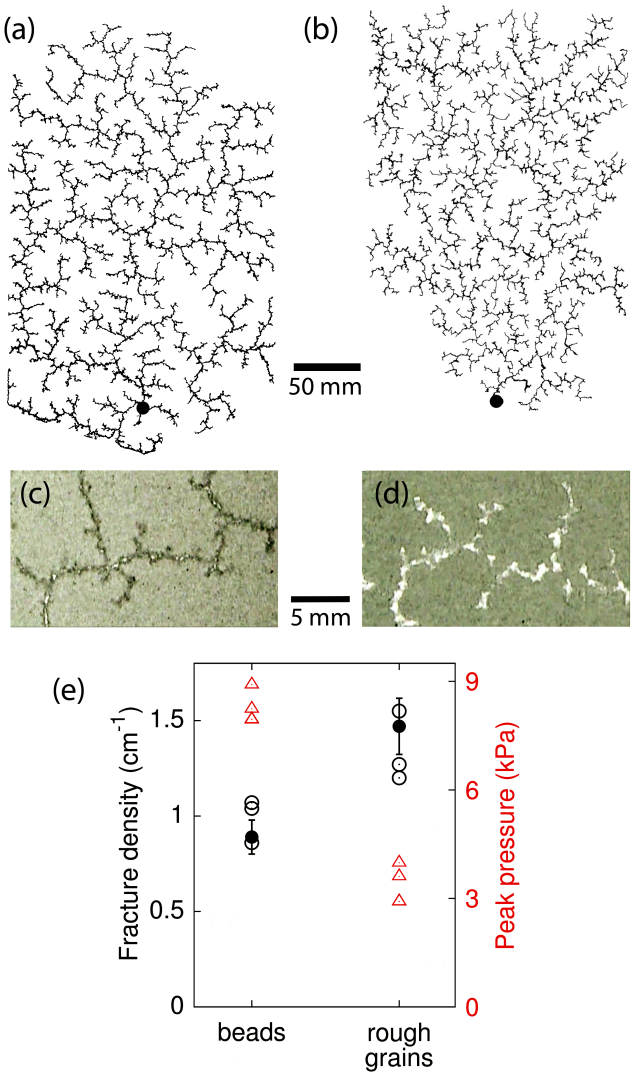

FIG. 11. Effect of grain shape. Full fracture patterns obtained for (a) spherical glass beads and (b) irregular grains sieved to the same 75–100 μm size range. Images (c) and (d) illustrate the difference in fracture width and appearance between the beads and irregular grains. The narrower fractures in the beads cause the back-illumination to scatter giving a dark appearance while the wider fractures for irregular grains allow the illumination straight through giving them a white appearance. (e) Measured fracture density (open circles), peak pressure (red triangles), and model results for fracture density predicted by Equation 7 (filled black circles), with each symbol representing a single experiment like those displayed in (a) and (b).

pressure is set by the capillary entry pressure as opposed to the frictional resistance of the material. The irregular shape of the grains creates larger pores, requiring lower gas pressure for capillary invasion as the precursor to fracturing. The effect of the higher frictional resistance is that thinner compaction fronts are required to balance a given capillary pressure. The higher fracture

density for irregular grains is thus a result of two separate effects: Larger pores means lower capillary pressure acting to expand the fracture, and higher friction means narrower compaction fronts are required to halt the expansion.

Another noticeable difference is that the irregular grains have wider fractures (mean fracture width of 0.72± 0.10 mm compared to 0.43± 0.10 mm for beads, see Figure 11 (c) and (d)). Recall that the width of the gas filled fracture can be estimated as $W = 2\Xi L$. Figure 10 shows that the compaction Ξ is over three times larger for the irregular grains, explaining the larger W despite the irregular grains having thinner compaction fronts L.

Analytical model for fracture density

The expected width of a compaction front may be estimated from the frictional properties of the granular material together with a simple model for stress transmission within the packing. Stress imposed on a granular medium propagates and disperses via grain-grain contacts. The capillary forces at the fracture boundary exert a stress on the interfacial grains with a mean component in the horizontal, in-plane direction. A significant portion of this stress gets redirected towards the confining plates, thus increasing the friction force [40]. We assume a Janssen relation that states that the out-of-plane stress σ_{zz} is proportional to the applied in-plane stress σ_{xx} by $\sigma_{zz} = \kappa\sigma_{xx}$, where κ is the Janssen coefficient, found in simulation to be 0.58±0.05 for spherical beads [61, 63]. The fracturing pressure P_F that needs to be applied at the fracture interface in order to displace the accumulation front increases exponentially with L according to the following relation, simplified to remove gravitational effects [40, 61]:

$$P_F = P_T \exp\left(2\mu\kappa\frac{L}{b}\right), \tag{4}$$

where μ is the static coefficient of friction (estimated, using the angle of repose as $\mu \approx \tan\alpha$), b is the plate spacing and P_T the threshold pressure at the far side of the front, i.e. the minimum pressure needed to compact the granular bed; this was taken as equal to the gravitational stress half-way between the plates, taking into account buoyancy and porosity, i.e.

$$P_T = \frac{1}{2}b\rho_e(1-n_0)g, \tag{5}$$

where ρ_e is the effective density of glass in water, n_0 is uncompacted porosity and g acceleration due to gravity.

Assuming that the compaction fronts are much wider than the internal width of the gas-filled fracture, spatial fracture density may be estimated simply as

$$D = \frac{1}{W+2L} \approx \frac{1}{2L}. \tag{6}$$

And as L may be estimated using Equation 4, and P_F may itself be estimated from grain size as in Equation 3, it follows that the spatial density of the fracture pattern may be estimated directly from the basic material properties μ, n, θ and d without reference to PIV results or pressure measurements. This final equation is as follows:

$$D = \frac{\mu\kappa}{b}\left(\ln\left[\frac{8a\gamma\cos\theta}{b\rho_e d(1-n)g}\right]\right)^{-1}, \tag{7}$$

where a is the prefactor from Equation 3, found to equal 2.0 for typical fracturing pressure. This value found for a only applies to the spherical beads, and a measured P_F of 3.1 kPa was used for the irregular grains in place of Equation 3.

The parameters relating to the frictional resistance of the compaction front; μ, κ and b are outside the logarithm in Equation 7 and are the parameters to which D is most sensitive. Figure 11 (e) compares predicted (Eq.(7)) and measured fracture densities. The model correctly predicts an increasing fracture density for the rough grains which is a result of higher friction and lower fracturing pressure producing narrower compaction fronts, allowing the fracture branches to approach each other closer. The model provides a close approximation to measured values, predicting fracture densities of 0.89 and 1.47 cm^{-1} (±10%) for the 75–100 μm beads and the irregular grains respectively, in agreement with measured values of 1.0 and 1.4 cm^{-1}. The close match is surprising given the simplicity of the model.

The parameters originating from the capillary stress exerted by the gas fracture on the granular packing (γ, θ, d) are less influential on the emerging fracture density D (being inside the logarithm). The model therefore explains the observed insensitivity of D as a function of grain size. The black line in Figure 8 (b) shows model results compared to measured D values (open circles), again reproducing the observed trend with a good match in values. Equation 7 predicts only a 10% increase in fracture density with grain size (including bead size dependence of porosity) over the range of sizes studied.

The capillary stress at the fracture interface is assumed proportional to $\gamma\cos\theta$ and is maximal for high gas-liquid surface tension and for perfectly wetting ($\theta = 0$) materials. A higher capillary stress at the interface allows the fractures to expand wider, growing larger compaction fronts separating the fractures, ultimately resulting in a lower fracture density D. Our experiments use highly wetting, hydrophilic grains ($\theta = 12°, \cos\theta = 0.98$). Previous studies have found wettability to significantly influence multiphase invasion patterns in fixed porous media models [64–66]. We have not investigated the effect of

wetting on the fracturing process, however, the assumptions of the model imply that fracturing is driven by the capillary forces exerted at the interface, which tend to zero for non-wetting conditions ($\theta = 90°$).

Dependence on gas injection rate

The rate of gas injection Q into 53–100 μm beads was varied across five orders of magnitude, from 0.001 to 100 mL/min. The collected results are presented in Figure 12. Figure 13 shows quantitative aspects of the same results.

From both images and graphs, it is clear that there is no significant variation with rate up to about 0.1 mL/min. This is the stick-slip regime described in the previous sections (outside this rate study all experiments were performed at 0.03 mL/min unless specified otherwise). The rate independence here is to be expected: as a threshold-limited process, the only influence of the rate is the length of time it takes for the pressure to build up to the next threshold, which likely has little influence on the pattern (see Figure 4).

From about 0.3 mL/min onwards, the pattern becomes strongly rate-dependent. Below this rate, the pressure during fracturing rises and falls in the stick-slip manner seen in Figure 4, but stays close to a constant fracturing pressure P_F during the whole experiment. Above this rate, after the first fractures appear close to P_F, the pressure continues to build, reaching a maximum and then falling off as the fractures approach the open end of the cell, with no discernible stick-slip fluctuations. This maximum pressure increases with increasing rate, as seen in Figure 13. There is thus a critical rate above which the growth dynamics becomes continuous rather than stick-slip.

As well as becoming continuous in time, the movement of the granular bed begins to extend much further from the fractures. At 0.1 mL/min and below, fractures open by means of local compaction as shown in Figures 6 and 7. Above this rate, they displace the grains globally rather than merely locally, as illustrated in Figure 14. Thus the transition to rate-dependent behaviour reflects a fundamental transition from fracturing of a solid-like, deformable packing, to gas invasion into a granular suspension.

The change in flow behaviour can be explained as a fluidisation transition: above a threshold flow rate Q_f the drag force will be sufficient to mobilise the grains and set the whole bed in motion. This concept has already been used to explain pattern transitions in part-filled bead beds [41] and tube geometries [67], and here we use the same approach; the bed will fluidise when the fluid pressure gradient ∇P is sufficiently large to overcome gravitational friction:

$$\nabla P > \mu \rho_e g \tag{8}$$

The fluid pressure gradient through the packing according to Darcy's Law [68] is

$$\nabla P = \frac{\eta Q_f}{kA} \tag{9}$$

where η is the viscosity, A the cell cross-sectional area and k the permeability, predicted for monodisperse spherical beads of diameter d by the Kozeny-Carman relation [51]

$$k = \frac{d^2}{180} \frac{n^3}{(1-n)^2} \tag{10}$$

where n is the porosity. From Equations 8 and 9 we can predict the critical fluidisation flow rate Q_f as

$$Q_f = \frac{\mu \rho_e g k A}{\eta} \tag{11}$$

In order to make the conclusion more general, we define a new dimensionless number F, the *Fluidisation number*, which is independent of cell dimensions. F is the ratio of viscous and frictional forces acting on the granular packing:

$$F = \frac{q\eta}{\mu \rho_e g k} \tag{12}$$

where $q = Q/A$ is the time- and space-averaged Darcy flow rate. F is equivalent to Q/Q_f, so for $F > 1$ (high injection rate) we expect the bed to be fluidised, and for $F < 1$ we expect to see stick-slip behaviour with no global movement of the grains. $F = 1$ marks the transition from a frictional regime at low injection rate (low capillary number) to a regime dominated by viscous forces at high flow rate (high capillary number).

Permeability was measured directly, as well as being calculated from equation (10), and were found to be in good agreement. Using these values with an estimated $\mu = \tan 32°$ from the tangent of the measured angle of repose, we predict $F = 1$ to occur at 0.2 mL/min for 53–100 μm beads. This value, marked on the graphs in Figure 13, is consistent with the flow rate at which the fluidisation transition is observed experimentally. Using the classical definition of the Capillary number, Ca= $\eta v/\gamma$, with seepage velocity $v = Q/(nA)$, we find the fluidization transition at Ca= 10^{-6}.

With a fluidised bed, grain displacement occurs globally rather than locally which explains the increasing directionality of fractures at high injection rates. At very high rates the fractures align with the streamlines of flow through the system (compare to Figure 14). In Figure 13, the increased directionality is expressed as a decreased tortuosity.

The fracture density increases at high rates; with viscous flow pushing the grains through the whole cell, the

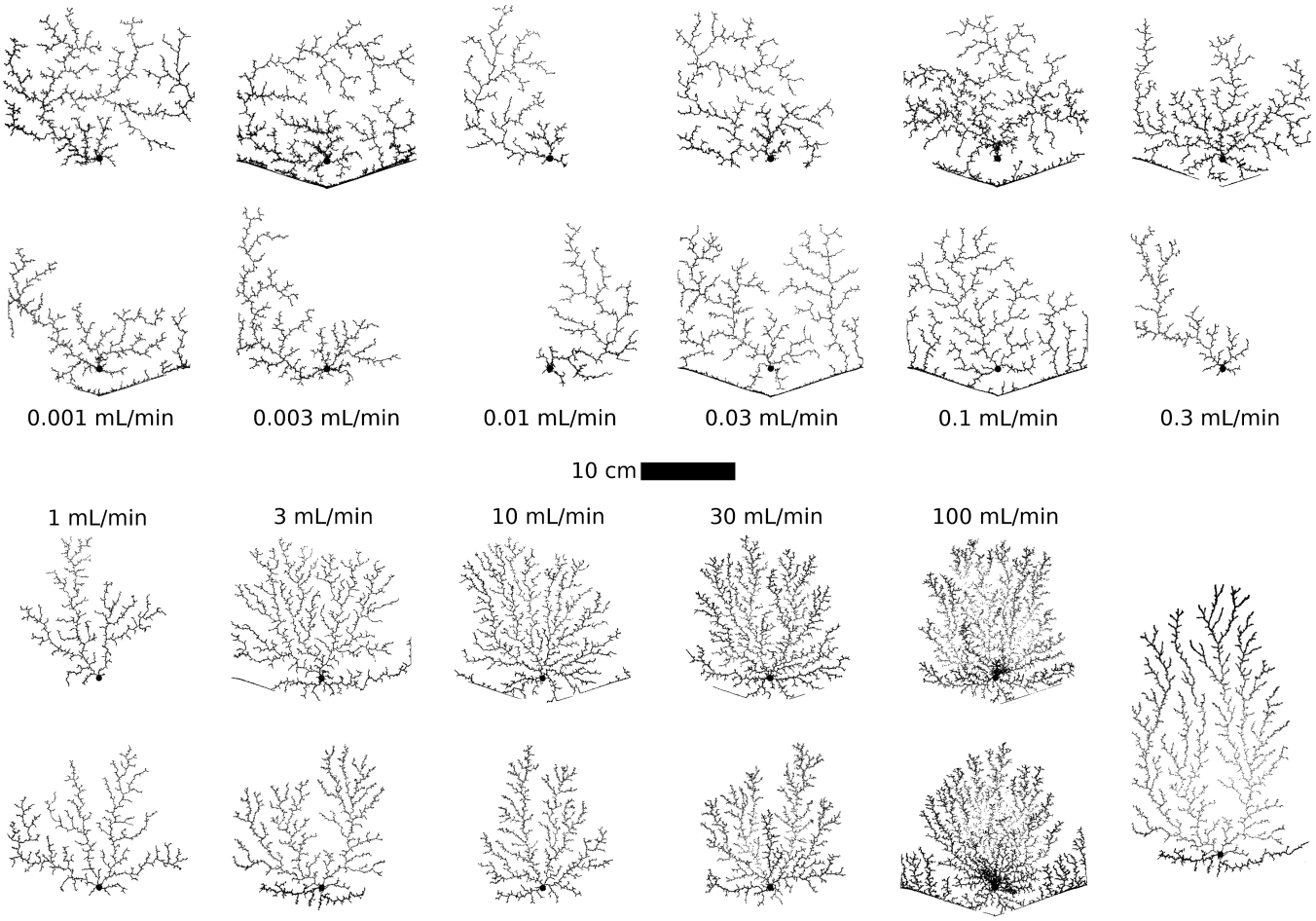

FIG. 12. Invasion patterns obtained for varying gas injection rates. The image in the bottom right shows a full invasion pattern for 3 mL/min.

spacing between fractures is no longer limited by the compression of the intermediate granular bed as discussed in the previous section. The mean cross-sectional area of the gas-filled fractures in contrast shows no clear trend with rate.

The images shown in Figure 12 are taken at the moment the fractures first reach 15 cm from the inlet. Within this first half of the cell the invading air channels at high rates still appear visually fracture-like. However in the second half of the cell the channels widen and take on the appearance of viscous fingers (bottom-right of Figure 12), similar to the morphologies observed in granular suspensions with lower granular filling fraction [14, 22].

It should be noted that this experiment was performed with an open boundary condition at one end of the cell, allowing movement of both grains and fluid. If instead the boundary permitted passage of fluid but not grains, then the stick-slip behaviour at $F < 1$ should remain unaffected but the behaviour at $F > 1$ might be markedly different in ways which are beyond the scope of this study [60].

One final rate dependence was seen only at the very highest rate, 100 mL/min. Whereas at lower rates the patterns, once formed, appear fixed and invariant, at this rate the fingers are sufficiently fluidised that they may deform or pinch closed after growth.

CONCLUSION

We have conducted an extensive series of experiments where saturated, cohesionless beds of granular material were fractured by forced injection of air. Gas-driven fracturing of granular suspensions and saturated packings occur in geological processes such as soil drying, sedimentary methane venting and magma degassing [1, 11, 13], and our results contribute to a deeper understanding of how the multiphase gas/liquid/grain interactions govern fracturing dynamics and emergent fracture network properties. Like previous studies (e.g. [6, 14, 22, 26]), we observe gas penetration in the form of fractures that open up conductive pathways through the saturated granular material. Fracturing occurs when fluid forces (capillary and viscous stress) overcome the deformational or

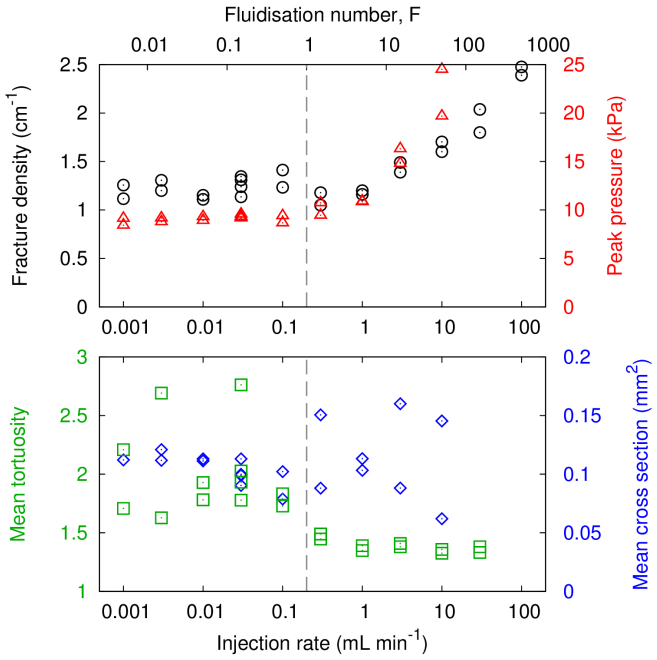

FIG. 13. Dependence of fracture pattern properties on injection rate. (black circles) fracture density; (red triangles) peak pressure; (green squares) mean tortuosity from inlet; (blue diamonds) mean fracture cross sectional area. Each symbol represents a single experiment. The dashed line indicates the estimated value of $F = 1$, the fluidisation transition.

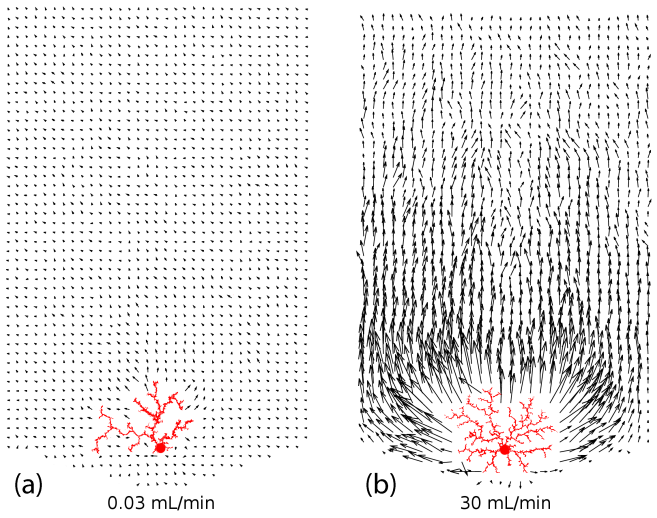

FIG. 14. Fluidisation transition. Whole-cell PIV showing net displacement of the granular bed exaggerated 50× at an early stage of growth for (a) 0.03 and (b) 30 mL/min. At low rate (a) there is no discernible grain movement except very close to the fractures; at high rate (b) the whole bed is fluidised and pushed through the cell. The width of the PIV fields correspond to the cell width, i.e. 200 mm.

frictional resistance of the material [6, 26]. We have found two distinct regimes in our experiments: a frictional regime at low gas injection rate, and a viscous regime at high injection rate.

In the frictional regime, the dynamics are dominated by stick-slip growth of fracture branches. A period of inactivity is followed by sudden fracturing, followed by another period of inactivity and so on. The pressure builds and drops in a saw-tooth fashion familiar from other intermittent systems such as frictional sliding [52] and earthquakes [53]. Several authors have pointed to intermittency in the opening/closing of fractures as a characteristic feature of both methane vents in sediments [5–8, 10] and gas conduits in magma [13–15]. Our results show that this large-scale intermittency is echoed in the small-scale, stick-slip intermittency in the growth of individual fractures, which we attribute to the nonlinear frictional response of the granular material.

PIV analysis of grain displacement reveals a compaction front surrounding the fractures (Figure 7). Our results show that it is ultimately the frictional resistance of this jammed compaction front that halts the lateral widening of the fractures, balancing the capillary stress exerted by the gas on the fracture interface. In a quasi-2D system like our Hele-Shaw cell, the friction is absorbed by the confining plates. It is at this point not clear whether a similar compaction process would take place in an unconfined 3D geometry, however we speculate that local compaction of material surrounding internally weakened conduits could increase the structural stability of gas migration pathways in sediments and crystal-rich magma.

The intermittent dynamics and the growth of the compaction front have implications for the fracturing pressure. The maximum pressure that the front can withstand is set by the capillary entry pressure of the pores of the compacted material. Below this pressure, the system responds to an increasing gas pressure by mobilizing friction (e.g. thickening the front). This means that nucleation of a new fracture length won't take place until the gas starts to penetrate the front by capillary invasion of the pores, triggering accelerated growth by locally fluidising the material. The pressure at the onset of fracturing is therefore determined by the capillary properties (pore size, wetting) of the material, and is independent of the frictional or deformational properties of the medium.

In engineering applications of pneumatic fracturing (e.g. soil remediation [18, 19], stimulation of hydrocarbon reservoirs [16, 17]), the objective is to increase the rate of fluid exchange with the bulk by generating a network of conductive paths. The rate of fluid exchange will to a large degree be determined by how closely spaced the fracture branches are, i.e. the spatial density of the network. The fractures in our experiments grow by tip-splitting to form a rooted binary tree network. The self-avoiding nature of the network, and the minimum separation distance between neighbouring branches is set by

the compaction fronts. Our experiments display a characteristic length scale: a fairly uniform separation distance between fracture branches, which we attribute to confinement effects (the cell has only one open edge), and "cooperative" fracturing in a local process zone. The resulting spatial fracture density is to a first approximation determined by the width of the gas-filled fracture and the compaction fronts either side ($D = (W + 2L)^{-1}$), where the thickness of the compaction front L depends on both granular friction and capillary pressure. Our experiments with irregular grains produced higher fracture density compared to smooth beads because: (1) higher friction gave narrower compaction fronts, and (2) larger pores gave lower fracturing pressure.

The change in dynamics from stick-slip frictional to continuous (viscous) invasion occurs as a result of a fluidisation transition [41, 67]: when the flow velocity of displaced fluid through the granular bed is high enough that viscous drag overcomes the friction between the grains and the cell, the entire granular bed is set in motion. The fractures grow into a partially fluidised bed, where granular material is pushed towards the open boundary. The fracturing process becomes rate-dependent, and we observe an increasing fracture density as a function of rate. We note the importance of the open boundary for this particular observation, and that work by other authors on granular displacement with closed boundaries for grain flow produce a different set of compaction dynamics [48, 60].

Our results show that multiphase flow and fracturing of granular materials is governed by a complex interplay between capillary, frictional and viscous forces, and we demonstrate the effect of material properties and local deformation on the emergent patterning of the evolving fracture network. While open questions remain regarding the fundamental forces at play, a big challenge for future work will be to incorporate more realistic subsurface conditions such as bulk 3D behaviour and heterogeneity to successfully model sedimentary venting and magma degassing dynamics, and to optimise pneumatic fracturing processes to achieve maximum fluid exchange rates, thereby reducing operation time and costs.

This work was supported in part by the Engineering and Physical Sciences Research Council (EP/L013177/1) and Sêr Cymru National Research Network in Advanced Engineering and Materials (NRN141). The authors thank Thaís Sousa de Sateles for preliminary tests.

* b.sandnes@swansea.ac.uk

[1] A. Groisman and E. Kaplan, An experimental study of cracking induced by desiccation, Europhys. Lett. **25**, 415 (1994).

[2] L. Goehring, Evolving fracture patterns: columnar joints, mud cracks and polygonal terrain, Phil. Trans. R Soc. A **371**, 20120353 (2013).

[3] L. Goehring, J. Li, and P. Kiatkirakajorn, Drying paint: from micro-scale dynamics to mechanical instabilities, Phil. Trans. R Soc. A **375**, 20160161 (2017).

[4] N. Shakhova, I. Semiletov, A. Salyuk, V. Yusupov, D. Kosmach, and O. Gustafsson, Extensive methane venting to the atmosphere from sediments of the east siberian arctic shelf, Science **327**, 1246 (2010).

[5] B. P. Boudreau, B. D. Johnson, I. Croudace, A. Reed, Y. Furukawa, K. M. Dorgan, P. A. Jumars, A. S. Grader, and B. S. Gardiner, Bubble growth and rise in soft sediments, Geology **33**, 517 (2005).

[6] A. K. Jain and R. Juanes, Preferential mode for gas invasion in sediments: Grain-scale mechanistic model of coupled multiphase fluid flow and sediment mechanics, J. Geophys. Res. **114**, B08101 (2009).

[7] M. Hovland, R. Heggland, M. H. De Vries, and T. I. Tjelta, Unit-pockmarks and their potential significance for predicting fluid flow, Mar. Petrol. Geol. **27**, 1190 (2010).

[8] L. M. Cathles, S. Zheng, and D. Chen, The physics of gas chimney and pockmark formation, with implications for assessment of seafloor hazards and gas sequestration, Mar. Pet. Geol. **27**, 82 (2010).

[9] G. Varas, V. Vidal, and J.-C. Geminard, Venting dynamics of an immersed granular layer, Phys. Rev. E **83**, 011302 (2011).

[10] B. P. Scandella, C. Varadharajan, H. F. Hemond, C. Ruppel, and R. Juanes, A conduit dilation model of methane venting from lake sediments, Geophys. Res. Lett. **38**, L06408 (2011).

[11] B. P. Scandella, K. Delwiche, H. F. Hemond, and R. Juanes, Persistence of bubble outlets in soft, methane-generating sediments, J. Geophys. Res. Biogeosci. **122**, 1298 (2017).

[12] A. Parmigiani, S. Faroughi, C. Huber, O. Bachmann, and Y. Su, Bubble accumulation and its role in the evolution of magma reservoirs in the upper crust, Nature **532**, 492 (2016).

[13] K. Cashman, R. S. J. Sparks, and J. D. Blundy, Vertically extensive and unstable magmatic systems: A unified view of igneous processes, Science **355**, 1280 (2017).

[14] J. Oppenheimer, A. C. Rust, K. V. Cashman, and B. Sandnes, Gas migration regimes and outgassing in particle-rich suspensions, Front. Phys. **3**, 60 (2015).

[15] J. Suckale, K. Cashman, and P. O. Persson, Flow-to-fracture transition in a volcanic mush plug may govern normal eruptions at stromboli, Geophys. Res. Lett. **43**, 2016GL071501 (2016).

[16] A. Rogala, J. Krzysiek, M. Bernaciak, and Hupka J, Non-aqueous fracturing technologies for shale gas recovery, Physicochem. Probl. Miner. Process. **49**, 313 (2013).

[17] R. Barati and J.-T. Liang, A review of fracturing fluid systems used for hydraulic fracturing of oil and gas wells, J. Appl. Polym. Sci. **131**, 40735 (2014).

[18] C. M. Christiansen, C. Riis, S. B. Christensen, M. M. Broholm, A. G, Christensen, K. E. S. Klint, J. S. A. Wood, P. Bauer-Gottwein, and P. L. Bjerg, Characterization and quantification of pneumatic fracturing effects at a clay till site, Environ. Sci. Technol. **42**, 570 (2008).

[19] U. Frank and Barkley N, Remediation of low permeability subsurface formations by fracturing enhancement of soil vapor extraction, J. Hazard. Mater. **40**, 191 (1995).

[20] A. J. Cavanagh and Haszeldine, The sleipner storage site:

Capillary flow modeling of a layered co2 plume requires fractured shale barriers within the utsira formation, Int. J. Greenh. Gas Control **21**, 101 (2014).

[21] A. Islam, S. Chevalier, I. B. Salem, Y. Bernabe, R. Juanes, and M. Sassi, Characterization of the crossover from capillary invasion to viscous fingering to fracturing during drainage in a vertical 2D porous medium, Int. J. Multiphase Flow **58**, 279 (2014).

[22] C. Chevalier, A. Lindner, M. Leroux, and E. Clément, Morphodynamics during air injection into a confined granular suspension, J. NonNewton. Fluid **158**, 63 (2009).

[23] X.-Z. Kong, W. Kinzelbach, and F. Stauffer, Morphodynamics during air injection into water-saturated movable spherical granulates, Chem. Eng. Sci. **65**, 4652 (2010).

[24] R. Holtzman and R. Juanes, Crossover from fingering to fracturing in deformable disordered media, Phys. Rev. E. **82**, 046305 (2010).

[25] H. Shin and J. C. Santamarina, Fluid-driven fractures in uncemented sediments: underlying particle-level processes, Earth Planet. Sc. Lett. **299**, 180 (2010).

[26] R. Holtzman, M. L. Szulczewski, and R. Juanes, Capillary fracturing in granular media, Phys. Rev. Lett. **108**, 264504 (2012).

[27] H. S. Hele-Shaw, On the motion of a viscous fluid between two parallel plates, Nature **58**, 34 (1898).

[28] P. G. Saffman and G. Taylor, The penetration of a fluid into a porous medium or Hele-Shaw cell containing a more viscous liquid, P. Roy. Soc. Lond. A Mat. **245**, 312 (1958).

[29] L. Paterson, Radial fingering in a hele-shaw cell, J. Fluid. Mech. **113**, 513 (1981).

[30] L. Paterson, Diffusion-limited aggregation and two-fluid displacements in porous media, Phys. rev. Lett. **52**, 1621 (1984).

[31] P. G. Saffman, Viscous fingering in Hele-Shaw cells, J. Fluid Mech. **173**, 73 (1986).

[32] G. M. Homsy, Viscous fingering in porous media, Ann. Rev. Fluid Mech. **19**, 271 (1987).

[33] C. Chevalier, A. Lindner, and E. Clément, Destabilization of a Saffman-Taylor fingerlike pattern in a granular suspension, Phys. Rev. Lett. **99**, 174501 (2007).

[34] Ø. Johnsen, C. Chevalier, A. Lindner, R. Toussaint, E. Clément, K. J. Måløy, E. G. Flekkøy, and J. Schmittbuhl, Decompaction and fluidization of a saturated and confined granular medium by injection of a viscous liquid or gas, Phys. Rev. E **78**, 051302 (2008).

[35] R. Toussaint, K. J. Måløy, Y. Méheust, G. Løvoll, M. Jankov, G. Schäfer, and J. Schmittbuhl, Two-phase flow: structure, upscaling, and consequences for macroscopic transport properties, Vadose Zone J. **11**, 3 (2012).

[36] H. Huang, F. Zhang, P. Callahan, and J. Ayoub, Granular fingering in fluid injection into dense granular media in a Hele-Shaw cell, Phys. Rev. Lett. **108**, 258001 (2012).

[37] F. Zhang, B. Damjanac, and H. Huang, Coupled discrete element modeling of fluid injection into dense granular media, J. Geophys. Res.-Sol. Ea. **118**, 2703 (2013).

[38] I. Ghani, D. Koehn, R. Toussaint, and C. W. Passchier, Dynamic development of hydrofracture, Pure Appl. Geophys. **170**, 1685 (2013).

[39] B. Sandnes, H. A. Knudsen, K. J. Måløy, and E. G. Flekkøy, Labyrinth patterns in confined granular-fluid systems, Phys. Rev. Lett. **99**, 038001 (2007).

[40] H. A. Knudsen, B. Sandnes, E. G. Flekkøy, and K. J. Måløy, Granular labyrinth structures in confined geometries, Phys. Rev. E **77**, 021301 (2008).

[41] B. Sandnes, E. G. Flekkøy, H. A. Knudsen, K. J. Måløy, and H. See, Patterns and flow in frictional fluid dynamics, Nat. Comm. **2**, 288 (2011).

[42] B. Sandnes, E. G. Flekkøy, and K. J. Måløy, Stick slip displacement of confined granular mixtures: bubble expansion, Eur. Phys. J.-Special Topics **204**, 19 (2012).

[43] G. Løvoll, Y. Méheust, R. Toussaint, J. Schmittbuhl, and K. J. Måløy, Growth activity during fingering in a porous Hele-Shaw cell, Phys. Rev. E **70**, 026301 (2004).

[44] K. T. Tallakstad, H. A. Knudsen, T. Ramstad, G. Løvoll, K. J. Måløy, R. Toussaint, and E. G. Flekkøy, Steady-state two-phase flow in porous media: statistics and transport properties, Phys. Rev. Lett. **102**, 074502 (2009).

[45] A. Ferrari, J. Jiminez-Martinez, T. Le Borgne, Y. Meheust, and I. Lunati, Challenges in modeling unstable two-phase flow experiments in porous micromodels, Water Resour. Res. **51**, 1381 (2015).

[46] J.-H. Choi, Y. Seol, R. Boswell, and R. Juanes, X-ray computed-tomography imaging of gas migration in water-saturated sediments: from capillary invasion to conduit opening, Geophys. Res. Lett. **38**, 17 (2011).

[47] K. E. Fauria and A. W. Rempel, Gas invasion into water-saturated, unconsolidated porous media: implications for gas hydrate reservoirs, Earth Planet. Sc. Lett. **312**, 188 (2011).

[48] F. K. Eriksen, R. Toussaint, A. L. Turquet, K. J. Måløy, and E. G. Flekkøy, Pneumatic fractures in confined granular media, Phys. Rev. E **95**, 062901 (2017).

[49] F. A. L. Dullien, Porous media: fluid transport and pore structure, Academic press, (2012).

[50] J. J. Cras, C. A. Rowe-Taitt, D. A. Nivens, and F. S. Ligler, Comparison of chemical cleaning methods of glass in preparation for silanization, Biosens. Bioelectron. **14**, 683 (1999).

[51] H.-J. Butt, K. Graf, and M. Kappl, Physics and chemistry of interfaces, John Wiley & Sons, (2006).

[52] M. Urbakh, J. Klafter, D. Gourdon, and J. Israelachvili, The nonlinear nature of friction, Nature **430**, 525 (2004).

[53] W. F. Brace and J. D. Byerlee, Stick-slip as a mechanism for earthquakes, Science **153**, 990 (1966).

[54] R. Fischer, P. Gondret, and M. Rabaud, Transition by intermittency in granular matter: from discontinuous avalanches to continuous flow, Phys. Rev. Lett. **103**, 128002 (2009).

[55] C.-H. Liu, S. R. Nagel, D. A. Schecter, S. N. Coppersmith, S. Majumdar, O. Narayan, and T. A. Witten, Force fluctuations in bead packs, Science **269**, 513 (1995).

[56] T. S. Majmudar and R. P. Behringer, Contact force measurements and stress-induced anisotropy in granular materials, Nature **435**, 1079 (2005).

[57] A. J. Liu and S. R. Nagel, Jamming is not just cool any more, Nature **396**, 21 (1998).

[58] V. Trappe, V. Prasad, L. Cipelletti, P. N. Segre, and D. A. Weitz, Jamming phase diagram for attractive particles, Nature **411**, 772 (2001).

[59] M. Van Hecke, Jamming of soft particles: geometry, mechanics, scaling and isostaticity, J. Phys.-Condens. Mat. **22**, 033101 (2010).

[60] F. K. Eriksen, R. Toussaint, K. J. Måløy, and E. G. Flekkøy, Invasion patterns during two-phase flow in de-

formable porous media, Front. Phys. **3**, 81 (2015).
[61] B. Marks, B. Sandnes, G. Dumazer, J. A. Eriksen, and K. J. Måløy, Compaction of granular material inside confined geometries, Front. Phys. **3**, 41 (2015).
[62] G. Mason and D. W. Mellor, Simulation of drainage and imbibition in a random packing of equal spheres, J. Colloid Interf. Sci. **176**, 214 (1995).
[63] H. A. Janssen, Versuche über getreidedruck in silozellen, Z. Ver. Dtsch. Ing. **39**, 1045 (1895).
[64] M. Trojer, M. L. Szulczewski, and R. Juanes, Stabilizing fluid-fluid displacements in porous media through wettability alteration, Phys. Rev. Appl. **3**, 054008 (2015).
[65] R. Holtzman and E. Segre, Wettability stabilizes fluid invasion into porous media via nonlocal, cooperative pore filling, Phys. Rev. Lett. **115**, 164501 (2015).
[66] B. Zhao, C. W. MacMinn, and R. Juanes, Wettability control on multiphase flow in patterned microfluidics, PNAS **113**, 10251 (2016).
[67] G. Dumazer, B. Sandnes, M. Ayaz, K. J. Måløy, and E. G. Flekkøy, Frictional fluid dynamics and plug formation in multiphase millifluidic flow, Phys. Rev. Lett. **117**, 028002 (2016).
[68] J. Bear, Dynamics of fluids in porous media, Elsevier, (1972).